Acta Biomaterialia 162 (2023) 266–277

Contents lists available at ScienceDirect

Acta Biomaterialia

journal homepage: www.elsevier.com/locate/actbio

Full length article

Lengthwise regional mechanics of the human aneurysmal ascending thoracic aorta

Samar A. Tarraf[a], Benjamin Kramer[b], Emily Vianna[b], Callan Gillespie[c], Emídio Germano[b], Kelly B. Emerton[b], Rouzbeh Amini[a,d], Robb Colbrunn[c], Jennifer Hargrave[e], Eric E. Roselli[b,c], Chiara Bellini[a,*]

[a] Department of Bioengineering, Northeastern University, 360 Huntington Ave., Boston, MA, 02125 USA
[b] Aortic Center, Department of Thoracic and Cardiovascular Surgery, Cleveland Clinic, Cleveland, OH, USA
[c] Department of Biomedical Engineering, BioRobotics and Mechanical Testing Core, Cleveland Clinic, Cleveland, OH, USA
[d] Department of Mechanical and Industrial Engineering, Northeastern University, 360 Huntington Ave., Boston, MA, 02125 USA
[e] Department of Cardiothoracic Anesthesiology, Cleveland Clinic, Cleveland, OH, USA

ARTICLE INFO

Article history:
Received 23 November 2022
Revised 16 February 2023
Accepted 15 March 2023
Available online 20 March 2023

Keywords:
Aortic root
Planar biaxial testing
Constitutive modeling
Inflation-extension kinematics
Aging

ABSTRACT

The prognosis of patients undergoing emergency endovascular repair of ascending thoracic aortic aneurysm (ATAA) depends on defect location, with root disease bearing worse outcomes than proximal or distal aortopathy. We speculate that a spatial gradient in aneurysmal tissue mechanics through the length of the ascending thoracic aorta may fuel noted survival discrepancies. To this end, we performed planar biaxial testing on 153 root, proximal, and distal segments of ATAA samples collected from 80 patients receiving elective open surgical repair. Following data averaging via surface fitting-based interpolation of strain-controlled protocols, we combined *in-vitro* and *in-vivo* measurements of loads and geometry to resolve inflation-extension kinematics and evaluate mechanical metrics of stress, stiffness, and energy at consistent deformation levels. Representative (averaged) experimental data and simulated *in-vivo* conditions revealed significantly larger biaxial stiffness at the root compared to either proximal or distal tissues, which persisted as the entire aorta stiffened during aging. Advancing age further reduced biaxial stretch and energy storage, a measure of aortic function, across all ATAA segments. Importantly, age emerged as a stronger predictor of tissue mechanics in ATAA disease than either bicuspid aortic valve or connective tissue disorders. Besides strengthening the general understanding of aneurysmal disease, our findings provide specifications to customize the design of stent-grafts for the treatment of ATAA disease. Optimization of deployment and interaction of novel endovascular devices with the local native environment is expected to carry significant potential for improving clinical outcomes.

Statement of significance

Elucidating the lengthwise regional mechanics of ascending thoracic aortic aneurysms (ATAAs) is critical for the design of endovascular devices tailored to the ascending aorta. Stent-grafts provide a less invasive alternative to support the long-term survival of ATAA patients ineligible for open surgical repair. In this study, we developed a numerical framework that combines semi-inverse constitutive and forward modeling with *in-vitro* and *in-vivo* data to extract mechanical descriptors of ATAA tissue behavior at physiologically meaningful deformation. Moving distally from the aortic root to the first ascending aortic branch, we observed a progressive decline in biaxial stiffness. Furthermore, we showed that aging leads to reduced aortic function and is a stronger predictor of mechanics than either valve morphology or underlying syndromic disorder.

* Corresponding author at: Department of Bioengineering, Northeastern University, 360 Huntington Ave., Boston, MA, 02125 USA.
E-mail address: c.bellini@northeastern.edu (C. Bellini).

https://doi.org/10.1016/j.actbio.2023.03.023
1742-7061/

1. Introduction

Thoracic aortic aneurysms are focal dilatations of the aortic wall that carry elevated risk of rupture and dissection. The current incidence of ruptured thoracic aneurysms is 1.6 per 100,000 persons/year and bears a mortality rate upwards of 90% [1,2]. Early identification of vulnerable individuals and proper clinical management of the aneurysm are crucial to prevent these life-threatening events [3].

While most thoracic aortic aneurysms occur sporadically, 20% of patients inherit a single gene mutation that predisposes them to the disease [4]. Heritable conditions linked to thoracic aneurysms encompass syndromic disorders across multiple organ systems (e.g., Marfan Syndrome, MFS; Loeys-Dietz Syndrome, LDS; vascular Ehlers-Danlos Syndrome, EDS) or simply manifest as a family history of the disease [3]. Genetically triggered aortopathies often involve the aortic root and the ascending thoracic aorta [5–7], which combined harbor 60% of all thoracic aneurysms [8]. Contributing to the tally, half of bicuspid aortic valve (BAV) patients present with aneurysms of the ascending aorta [9]. The disparate etiology of ascending thoracic aortic aneurysms (ATAAs) motivates probing for both common traits and distinctive features across disease manifestations. Besides measuring higher strength in aneurysmal tissues from BAV patients compared with tricuspid aortic valve (TAV) peers [10–13], early evidence revealed differences in the microstructural and mechanical properties of the aneurysmal wall between MFS and non-MFS cohorts [14–16]. Proper interpretation of these findings hinges on further considerations regarding the age at which the disease manifests in each etiological group, given that aging alone contributes to both tissue and structural stiffening of the aortic wall [17–19].

Standard treatment for ATAA disease is open surgical repair to replace native tissues with a prosthetic vascular graft. While the outcomes of this procedure are generally favorable, 8–20% of patients with acute type A dissection are deemed too high risk [20,21] and would benefit from a less invasive endovascular placement of a stent-graft in support of weakened tissues. Notwithstanding this need, there is currently no device with FDA approval for the thoracic endovascular aortic repair (TEVAR) of ATAA aortopathy. Clinical reports describing either trials of investigational stent-grafts or off-label use of commercial devices often classify the entire length of the ascending thoracic aorta as a single landing zone (i.e., the location of stent-graft attachment), extending from the sinotubular junction to the proximal branching of the innominate artery [22]. Motivated by clinical outcomes, our team has recently emphasized the need to further partition the ascending thoracic aorta (referred to as Zone 0) into three segments: Zone 0A or the aortic root, Zone 0B or the proximal half of the ascending aorta, from the distal coronary ostia to the right main pulmonary artery, and Zone 0C or the distal half, past the right main pulmonary artery [21]. Leveraging this modified classification, we have shown that, among the recipients of emergency ascending TEVAR, patients with root disease experience significantly worst outcomes than those with proximal or distal disease, with age acting as an additional independent predictor of mortality [21].

These clinical findings suggest that regional differences—yet to be explored—through the length of the aneurysmal ascending thoracic aorta may complement the well established circumferential variation in structural and mechanical properties between the anterior and posterior regions [23–25]. The lengthwise mechanical characterization of ATAA tissues thus becomes imperative for the design of dedicated stent-graft devices that optimize deployment and interaction with the native environment by accounting for the response of the specific landing zone. Toward this end, we have recently shown that the elastic energy storage under equibiaxial loading increases from the aortic root to the distal segment, prompting the need to further explore the regional mechanics of ATAA tissues [26].

To minimize assumptions on loading conditions and extract mechanical metrics at physiologically meaningful deformation levels, we have developed a numerical framework that combines *in-vitro* testing with *in-vivo* imaging and pressure measurements. Following this approach, we report here the first mechanical characterization of aneurysmal tissues through the length of the ascending thoracic aorta, according to our revised classification of Zone 0 [21]. Leveraging a diverse cohort of patients, we further evaluate the extent to which age and patient medical history, including valve morphology and syndromic disorder, contribute to tissue mechanics.

2. Materials & methods

2.1. Patient population

All research activities on human subjects received Institutional Review Board approval at the Cleveland Clinic (#16-900, approved 8/1/2016). Following written informed consent for data collection and publication, 80 adults undergoing elective replacement of ascending thoracic aortic aneurysm (ATAA) were prospectively enrolled in the study and assigned to one of three mutually exclusive etiological groups: (1) patients with a bicuspid aortic valve (BAV), (2) patients with normal (tricuspid) aortic valve morphology suffering from a connective tissue disorder (CTD), and (3) patients with normal (tricuspid) aortic valve morphology without any known heritable condition predisposing to ATAA disease (TAV). Based on the relationship between age and ATAA function recently reported by our team [26] and accounting for the age at which the disease typically occurs with each predisposing factor, we further identified young (<40 year old), middle-aged (40 to 60 year old), and older (>60 year old) patient cohorts. Demographic data on the subjects included in the study and information on the average maximum diameter of the ATAA for each etiological group are listed in Table 1. Since no statistically significant differences emerged between male and female patients, data from both sexes were combined. Furthermore, since our analysis is intended to aid the design of endovascular devices that exclusively interact with ATAA tissues and on account of specimen availability, we did not pursue any comparison with age-matched, non-aneurysmal controls. Finally, although hypertension is a known risk factor for aneurysmal disease [3,27,28] and despite the prevalence (41/80 patients) of hypertension within our cohort, no comparisons were conducted to ascertain the independent effect of elevated blood pressure on ATAA mechanics, as most patients received antihypertensive treatment.

2.2. Planar biaxial testing

Sample Preparation. A total of 153 square tissue samples were carved from root (Zone 0A), proximal (0B), and distal (0C) segments [21] along the greater curvature of resected ATAAs, using a 15×15 mm^2 cutter with edges aligned to the anatomical circumferential and axial directions. Thickness was measured with a custom-built device at five locations across each specimen and averaged [26]. Tissues were either tested fresh or fast-frozen, to minimize changes in mechanical properties when same day testing could not be performed [29,30]. Frozen samples were preserved at -80°C and thawed overnight in 4°C normal saline ahead of testing.

Experimental Apparatus. Mechanical testing was performed with a customized planar biaxial system equipped with four motors (ADMET; Norwood, MA, USA) following established protocols [26,31–36]. A speckle pattern of India ink was applied via a rubber stamp onto the intimal side of tissues. Specimens were

Table 1
Characteristics of the patients enrolled in our study. Total number of patients, average (±SEM) and median patient age, number and percentage of female patients, average (±SEM) and median maximum ATAA diameter, as well as number and percentage of aortas that were frozen ahead of testing are reported for the mutually-exclusive BAV, CTD, and TAV etiological groups. Aortic size as measured from CT scans according to the centerline method [26].

etiology	n	age (yrs)		female sex		max diam. (cm)		frozen	
BAV	41	50.0±2.3,	52	13,	31.7%	4.71±0.12,	4.86	8,	19.5%
CTD	17	32.2±2.4,	31	7,	41.2%	4.71±0.13,	4.64	3,	17.6%
TAV	22	60.5±2.8,	61	5,	22.7%	5.05±0.14,	5.08	5,	22.7%

loaded onto the device using five equally spaced rakes along each edge, to yield a 10×10 mm^2 testing area. Anatomical circumferential and axial directions were aligned with in-plane loading axes 1 and 2, respectively (Fig. S1A). Tissue hydration was maintained by submersion into a heated saline bath at 37°C. A preload of 0.05N was applied to remove residual buckling. The displacement of the speckle pattern was recorded for calculation of in-plane Green-Lagrange strains via digital image correlation (VIC-2D Digital Image Correlation system v6.0.6, Correlated Solutions; Irmo, SC, USA).

Testing Protocols. Tissue samples were first tested under global stretch ratios of 1:1 (equibiaxial displacement of the loading arms in the circumferential and axial directions, performed as first and last), 1:0.75, 1:0.5, 0.5:1, and 0.75:1. This set of six biaxial protocols was repeated 3x sequentially and with no interruptions at increasing values of maximum global stretch (+0.1) or until tissue failure. Initial maximum global stretch was set to 1.4 for most proximal and distal samples, and to 1.3 for the root and other samples that were perceived as fragile or were expected to rupture at lower deformation. Tissue was preconditioned for nine cycles in the first equibiaxial protocol of the set with the lowest maximum global stretch, four cycles in the first equibiaxial protocol of each subsequent set, and two cycles in all remaining protocols, with data collected on the following and last cycle. This preconditioning strategy ensured repeatable responses while avoiding damage to the tissues due to prolonged testing duration. Without further tissue manipulation, samples were then held at a fixed global stretch along one axis and cyclically deformed along the orthogonal direction, up to a maximum global stretch of either 1.3 or 1.4. Global stretch was applied at a quasi-static loading rate of 0.5 mm/s. Traces of all protocols implemented during biaxial testing, including preconditioning cycles, are illustrated in Fig. S2.

2.3. Biaxial data analysis

Negligible in-plane shear [37] prompted mapping of the reference into the current, deformed configuration as $x_1 = \lambda_1 X_1,\ x_2 = \lambda_2 X_2,\ x_3 = \lambda_3 X_3$, where X_I $(I = 1, 2, 3)$ and x_i $(i = 1, 2, 3)$ are the reference and current coordinate sets, respectively, and λ_j $(j = 1, 2, 3)$ are the principal stretches aligned with the three anatomical directions of the aorta — circumferential, axial, and radial. The corresponding deformation gradient tensor $\boldsymbol{F} = \partial \boldsymbol{x}/\partial \boldsymbol{X}$ admits matrix representation diag$[\lambda_1, \lambda_2, \lambda_3]$ in our reference system. Similarly, matrix diag$[({\lambda_1}^2 - 1)/2, ({\lambda_2}^2 - 1)/2, ({\lambda_3}^2 - 1)/2]$ represents the Green-Lagrange strain tensor $\boldsymbol{E} = (\boldsymbol{C} - \boldsymbol{I})/2$, where $\boldsymbol{C} = \boldsymbol{F^T F}$ is the right Cauchy-Green deformation tensor, superscript T indicates the transpose, and $\boldsymbol{I}$ is the identity tensor. Experimental measures of in-plane Green-Lagrange strains facilitated calculation of in-plane stretches as $\lambda_1 = \sqrt{2E_{11} + 1}$ and $\lambda_2 = \sqrt{2E_{22} + 1}$, while λ_3 was determined by enforcing incompressibility through $J = \det(\boldsymbol{F}) = \lambda_1\lambda_2\lambda_3 = 1$.

Noting that that the top and bottom surfaces of tissue samples are traction-free and the thickness is smaller compared to in-plane dimensions, the first Piola-Kirchhoff stress tensor $\boldsymbol{P}$ assumes matrix form diag$[f_1/(L_2 H), f_2/(L_1 H), 0]$, where f_1 and f_2 are the forces measured by the load cells, L_1 and L_2 are the undeformed rake-to-rake distances delimiting the testing area, and H is the undeformed thickness. The second Piola-Kirchhoff stress tensor is then obtained as $\boldsymbol{S} = \boldsymbol{F^{-1}P}$ and represented by matrix diag$[P_{11}\lambda_2\lambda_3, P_{22}\lambda_1\lambda_3, 0]$.

2.4. Biaxial data averaging

Since our biaxial testing approach controlled for the displacement of the loading arms and considering that the maximum global displacement imposed in each test changed according to the protocol or if the tissue failed prematurely, measured local strains varied substantially across ATAA samples. To facilitate data averaging and fair inter-group comparison, we fit biquintic Hermite surface elements to second Piola-Kirchhoff stress data in the Green-Lagrange strain plane [38,39], and interpolated strain-controlled responses up to set loading conditions [18,25,40] (Fig. S1B).

Surface Fitting. Experimental data in the E_{11}, E_{22} plane (independent variables) were mapped onto the $\xi, \eta \in \{-1, 1\}$ domain assuming a single bilinear element (Eqs. (S1) and (S2)). The distribution of stress (dependent variable, either S_{11} or S_{22}) in the ξ, η plane was captured with a four-node biquintic element (Fig. S1B). Six shape functions were defined (Eq. (S3)) to estimate the nodal stress, alongside its first, second, and cross derivatives with respect to ξ and η. The stress at point p of coordinates (ξ_p, η_p) was approximated as

$$\hat{S}_p(\xi_p, \eta_p) = {N_i}^{jk}(\xi_p, \eta_p){S_i}^{jk}, \tag{1}$$

where ${N_i}^{jk}$ are the values of the shape functions at p and ${S_i}^{jk}$ are the values of the stress and its derivatives at node i, with i=1:4 for the node number and j, k=0:2 for the orders of the derivative, excluding j+k> 2 to reduce the total number of nodal values from 36 to 24. The twenty four ${S_i}^{jk}$ values were estimated by minimization (fminunc function; Matlab R2021a; Mathworks, Natick, MA) of the error function

$$E(S) = \sum_{p=1}^{n} |\hat{S}_p - S_p|^2 + \int\int G(S) d\xi d\eta, \tag{2}$$

where the first term is the least square solution for n data points and the second term is the double integral of the Sobolev norm (Eq. (S4)) for smoothing regions of sparse or noisy data [38,41–43], with S_p indicating experimental data and $\hat{S}_p$ approximated values from Eq. (1). Quality of fit relied upon the coefficient of determination

$$R^2 = 1 - \frac{\sum_{p=1}^{n} (S_p - \hat{S}_p)^2}{\sum_{p=1}^{n} (S_p - \bar{S})^2}, \tag{3}$$

where $\bar{S}$ is the mean of the experimental measures.

Data Interpolation. Leveraging nodal ${S_i}^{jk}$ values specific to each sample, we applied Eq. (1) to extract five strain-controlled data sets with standard E_{11} to E_{22} ratio of 1:1, 1:0.75, 1:0.5, 0.5:1, and 0.75:1, up to the largest experimental strain experienced by the least distensible tissue within each group (Fig. S1B).

Data Averaging. Given the nonlinear stress-strain behavior of ATAA tissues, proper averaging of experimental data is necessary to estimate group representative material parameters [37,44–46]. Average data sets were generated by calculating the mean and dispersion across samples of interpolated S_{11} and S_{22} values, at set E_{11} and E_{22} levels within the interpolation domain, and for each strain ratio protocol. Average Cauchy stress vs. stretch data sets were then obtained by applying $\boldsymbol{\sigma} = \boldsymbol{FSF}^T$.

2.5. Constitutive parameter estimation

Aneurysmal tissue was modeled as a hyperelastic material endowed with a strain energy density potential in the form

$$W = \frac{\mu}{2}(I_{\boldsymbol{C}} - 3) + \frac{c}{2}(e^{Q} - 1), \tag{4}$$

where $I_{\boldsymbol{C}} = {\lambda_1}^2 + {\lambda_2}^2 + {\lambda_3}^2$ is the first invariant of $\boldsymbol{C}$ with principal stretch directions 1,2,3 aligned with the anatomical circumferential, axial, and radial directions, μ (dimension of a stress) is a Neo-Hookean material parameter describing the isotropic contribution of the ground matrix, $Q = a_1{E_{11}}^2 + a_2{E_{22}}^2 + 2a_3E_{11}E_{22}$ is a quadratic form in the components of $\boldsymbol{E}$, and c (dimension of a stress) and a_1, a_2, a_3 (non-dimensional) are Fung-type material parameters often used to capture the anisotropic behavior of collagen fibers in ATAA tissues [25,47,48]. For such a material, the second Piola-Kirchhoff stress tensor is obtained as

$$\boldsymbol{S} = -p\boldsymbol{C}^{-1} + \frac{\partial W(\boldsymbol{E})}{\partial \boldsymbol{E}}, \tag{5}$$

where p is a Lagrange multiplier to enforce incompressibility. Best fit estimates of the 5 material parameters were obtained from the nonlinear least square minimization of the Euclidean norm of the error vector

$$e = \left[\frac{\hat{S}_{11} - S_{11}}{\bar{S}_{11}}; \frac{\hat{S}_{22} - S_{22}}{\bar{S}_{22}}\right], \tag{6}$$

where S is the experimental stress, $\hat{S}$ is the theoretical stress from Eq. (5), and $\bar{S}$ is the average experimental stress in either the circumferential or axial direction. Goodness of fit was expressed as root-mean-square-error (RMSE). Identification of constitutive parameters was performed on individual specimens as well as group average data sets.

2.6. In-vivo *mechanics modeling*

One of the main challenges of predicting the mechanical behavior of nonlinear tissues is that energy, stress, and stiffness depend on the deformation. With regard to ATAA disease, the scarcity of data describing *in-vivo* and traction-free geometries hinders accurate estimation of tissue strains under physiological loads. To overcome this hurdle while minimizing kinematics assumptions, we leveraged a property by which arteries preserve axial force independent of pressure when extended to their crossover axial stretch [49]. That is, the crossover axial stretch marks the intersection of axial force *vs.* axial stretch curves under different luminal pressures (Fig. S1D). Since operating above this limit is energetically sub-optimal, we assumed crossover axial stretch at systole, when the contraction of the heart imposes the largest axial deformation on ascending aortic tissues. We then leveraged experimental measures of traction-free thickness, systolic luminal radius, and systolic pressure to estimate the traction-free outer radius of ATAA samples and determine *in-vivo* circumferential stretch under inflation-extension kinematics, as detailed in loops 1–3 below (Fig. S1C).

Experimental Input. For a subset of patients (59 out of 80), the luminal radii of root, proximal, and distal ATAA segments were measured intraoperatively under systolic and diastolic loads, using epiaortic (EA) and transesophageal (TEE) imaging. EA and TEE ultrasound was performed following sternotomy but prior to any intervention, to preserve the integrity of ATAA tissues. Anatomical landmarks facilitated identification of desired ATAA segments for image capturing. Blood pressure was monitored continuously during surgery via an arterial line, and recorded at the time of imaging. Additional details on the methods for *in-vivo* data measurement are reported in the Supplementary Material.

Inflation-Extension Kinematics. The (R, Θ, Z) traction-free configuration of a pressurized and axially extended cylinder is mapped into the (r, θ, z) current configuration as $r = r(R)$, $\theta = \Theta$, $z = \lambda_z Z$ and admits a deformation gradient tensor $\boldsymbol{F}$ in the form $\mathrm{diag}[\partial r/\partial R, r/R, \lambda_z]$, where λ_z is the axial stretch. Assumption of incompressibility supports transformation of any reference radial position into the current configuration through $r = \sqrt{r_i^2 + (R^2 - R_i^2)/\lambda_z}$, where the subscript i denotes the luminal radius. Given best fit parameters for the strain energy density function in Eq. (4), the Cauchy stress tensor for any given deformation reads

$$\boldsymbol{\sigma} = -p\boldsymbol{I} + \boldsymbol{F}\frac{\partial W(\boldsymbol{E})}{\partial \boldsymbol{E}}\boldsymbol{F}^T, \tag{7}$$

where p is a Lagrange multiplier.

Algorithm for R_o and $\lambda_{z,co}$ Estimation.

LOOP 1: Accounting for the experimental measures of luminal radius at systolic pressure and traction-free tissue thickness, we resolved inflation-extension kinematics for a range of admissible axial stretches, to estimate the corresponding traction-free outer radius (Fig. S1C). Solution of radial equilibrium provided a theoretical value for the luminal pressure

$$P = \int_{r_i}^{r_o} \frac{1}{r}(\sigma_{\theta\theta} - \sigma_{rr})\, dr \tag{8}$$

where the subscript o indicates the outer radius. Estimates of R_o that minimized the difference between theoretical and given luminal pressure for each instance of λ_z were iteratively refined via the Newton-Raphson method.

LOOP 2: For each pair of R_o and λ_z, we resolved inflation-extension kinematics to identify the crossover axial stretch (Fig. S1C). Newton-Raphson was applied to determine the set of r_o values that accommodated luminal pressures between 10 and 140 mmHg, as calculated from Eq. (8). Solution of global axial equilibrium provided the corresponding axial force

$$f_z = \pi \int_{r_i}^{r_o} (2\sigma_{zz} - \sigma_{\theta\theta} - \sigma_{rr}) r\, dr \tag{9}$$

The crossover axial stretch ($\lambda_{z,co}$) was extracted from the intersection of axial force vs. axial stretch data sets under different luminal pressures (Fig. S1D).

LOOP 3: After updating R_o based on the identified crossover axial stretch, we repeated LOOP 2 to ensure that the $\lambda_{z,co}$ compatible with the revised traction-free dimensions deviated by $<1\%$ from the previous estimation (Fig. S1C).

Energy, Stress, and Stiffness Calculation. Estimates of R_o and $\lambda_{z,co}$ allowed calculation of systolic circumferential stretch as $\lambda_\theta = r/R$. Upon solving for local deformation, elastic energy (W, Eq. (4)), Cauchy stress ($\boldsymbol{\sigma}$, Eq. (7)), and linearized stiffness were evaluated at equispaced radial locations between the luminal and outer radii. The components of the linearized stiffness tensor were determined according to the small-on-large deformation approach [50]

$$C_{ijkl} = \sigma_{il}\delta_{jk} + \sigma_{lj}\delta_{ik} + F_{iI}F_{jJ}F_{kK}F_{lL}\frac{\partial^2 \hat{W}(\boldsymbol{E})}{\partial E_{IJ}\partial E_{KL}}, \tag{10}$$

where δ is the Kronecker delta, $(i, j, k, l) \equiv (r, \theta, z)$ and $(I, J, K, L) \equiv (R, \Theta, Z)$. We also evaluated tissue anisotropy through index $A =$

$0.5 \cdot (\lambda_{z,co} - \lambda_\theta)/(\lambda_{z,co} + \lambda_\theta)$ [19]. Noting that constitutive parameters from planar biaxial data describe homogenized tissue behavior (i.e., neglecting the layered structure of the aortic wall), we obtained and report the through-thickness integral mean of all mechanical metrics.

Model Evaluation. To assess the predictive capability of our modeling framework, we first compared estimates of traction-free inner radius with experimental measurements collected in a subset of ATAA samples. Freshly-harvested tissues were submerged en-bloc in saline solution within a 1×1 cm^2 grid container for imaging of distal and proximal edges. With the grid pattern for scaling, the luminal perimeter of the aorta was manually traced (roipoly function, Matlab v2021a; MathWorks, Natick MA) to measure the area (bwarea function, Matlab v2021a; MathWorks, Natick MA) and calculate the equivalent radius.

Second, we compared the through-thickness integral mean of predicted circumferential stress at systolic pressure and crossover axial stretch against the values that Koullias et al. [51] inferred under membrane assumption and for pressures of 100 and 220 mmHg, as a function of ATAA size measured through EA echocardiography.

Third, we compared predicted cyclic (diastole to systole) biaxial strains to reported measurements in both ATAA disease [52] and aged but non-aneurysmal ascending aortas [53]. We solved inflation-extension kinematics (Figs. S1C) to match the luminal diameters determined from imaging of diastolic and systolic configurations, assuming that tissues experienced crossover axial stretch during cardiac systole. Cyclic (area) circumferential strain was calculated as $100 \cdot (\pi {r_{i,sys}}^2 - \pi {r_{i,dia}}^2)/(\pi {r_{i,dia}}^2)$ and axial strain as $100 \cdot (\lambda_{z,sys} - \lambda_{z,dia})/\lambda_{z,dia}$, where subscripts *sys* and *dia* refer to systole and diastole, respectively.

2.7. Statistics

All values are reported as mean ± standard error of mean (SEM). Differences in mechanical metrics across groups were determined via one-way non-parametric Kruskal-Wallis test with Bonferroni correction for multiple comparisons. We further relied on non-parametric Spearman's rank-order correlation to evaluate the relationship between mechanical metrics and aging, where r_s describes the strength and direction of the correlation.

3. Results

Average Cauchy stress vs. stretch data for ascending thoracic aortic aneurysm (ATAA) tissues as a function of anatomical location, patient age, and underlying condition exhibited the expected transition from a low-stiffness response, capable of accommodating large deformations within a small stress range, toward a high-stiffness behavior of rapidly increasing stress upon further stretching (Figs. 1–2). Best fit material parameters that describe the average response for regional, chronological, and etiological groups with no less than 4 samples are reported in Table S1.

Within the bicuspid aortic valve (BAV) cohort and up to a stretch of 1.4, the root of young patients experienced larger circumferential distensibility and axial extensibility compared to proximal and distal samples under equibiaxial loading (Fig. 1A), though this relationship reversed with age (Fig. 1B,C). Furthermore, the average biaxial response of proximal ATAA tissues did not differ from that of the distal segment in the youngest (Fig. 1A) and oldest patients (Fig. 1C), at least within the experimental range of stretches, though it approached the behavior of the root in the middle age group (Fig. 1B). These findings reflect the differential effect of aging on the three anatomical regions of ATAA samples in the presence of BAV. While the root experienced the largest progressive decrease in distensibility and extensibility with age (Fig. 2A), the most substantial changes in the mechanics of proximal ATAA tissues occurred between the young and middle age group, after which the biaxial response stabilized (Fig. 2B). Note that distal tissues in the oldest age group were not stretched beyond the initial low-stiffness behavior, hence more information is necessary to fully characterize the mechanical response of this segment (Fig. 2C).

Amongst patients suffering from a connective tissue disorder (CTD), the root appeared less distensible than proximal tissues even in the young age group (Fig. 1D). Given that syndromic aortopathies are often characterized by highly penetrant root aneurysms and manifest earlier in life, we did not have enough samples to generate average curves for the distal region at any time point nor for any patient above 40 years of age, thus the effect of aging could not be investigated for this etiological group.

Within the cohort of patients that had no prior connective tissue disorder diagnosis and exhibited normal valve morphology (TAV), the root was less distensible and extensible than the proximal and distal regions in the middle age group (Fig. 1E), though differences within the low-stiffness response faded beyond age 60 (Fig. 1F). These findings echo more substantial changes in the mechanical behavior of the proximal (Fig. 2E) and distal segments (Fig. 2F) with age, at least in the circumferential direction, compared to the root (Fig. 2D).

To extract quantitative information on the mechanical function of ATAA tissues, we supplemented the comparison of interpolated equibiaxial responses (Figs. 1–2) by solving inflation-extension kinematics to recapitulate *in-vivo* measures of systolic pressure and luminal diameter, under the assumption of energetically-optimal crossover axial stretch (Figs. S1D). We resorted to the crossover axial stretch to compare ATAA tissues at analogous deformed configurations that approach their *in-situ* state [12,49]. Substantiating the validity of our approach, predicted values of traction-free luminal radii deviated by at most 20% from perioperative measurements on resected tissues from a subset of patients, with the majority of the estimates exhibiting $<$10% error (Fig. 3A). Given the inherent challenge of extracting reliable size information from digital images of flaccid tissues, our model predicted the traction-free geometry of ATAA samples with reasonable accuracy. Interestingly, a ±20% deviation from the estimated traction-free luminal radius did not alter the predicted crossover axial stretch, which therefore emerged as a robust property of ATAA tissues rather than geometry (Fig. S4). Furthermore, through-thickness integral means of calculated circumferential Cauchy stress under systolic luminal pressure and crossover axial stretch (average: 0.31±0.01 MPa) fell within the expected range for ATAA tissues at given diameters and for luminal pressures between 100 and 220 mmHg [51] (Fig. 3B). Finally, average cyclic circumferential (11.1±0.6%, measured from imaging) and axial (7.6±0.8%, predicted by the model) strains in proximal and distal ATAA tissues within our patient cohort fell within less than half a standard deviation of average *in-vivo* measurements acquired through ECG-gated CT scans in ATAA patients [52] and MR imaging in older individuals [53] (Fig. 3C).

Leveraging our model, we first compared regional properties independently of additional risk factors. While all three segments endured comparable circumferential stretch levels (Fig. 4D), the root displayed lower crossover axial stretch (1.29±0.02) than either proximal (1.37±0.03) or distal (1.39±0.03; $p < 0.05$; Fig. 4A) tissues, albeit only the latter was significant. Given this trend, and because the circumferential stretch was larger than the axial stretch in most samples, the average anisotropy index remained negative in all three regions, yet it approached zero in distal segments, where the mechanical response under *in-vivo* loads turned fairly isotropic (Fig. 4G). Wall thickness increased from root (0.95±0.04 mm) to distal tissues (1.14±0.05 mm; $p < 0.01$; Fig. 4H) and contributed to reducing the circumferential stress in

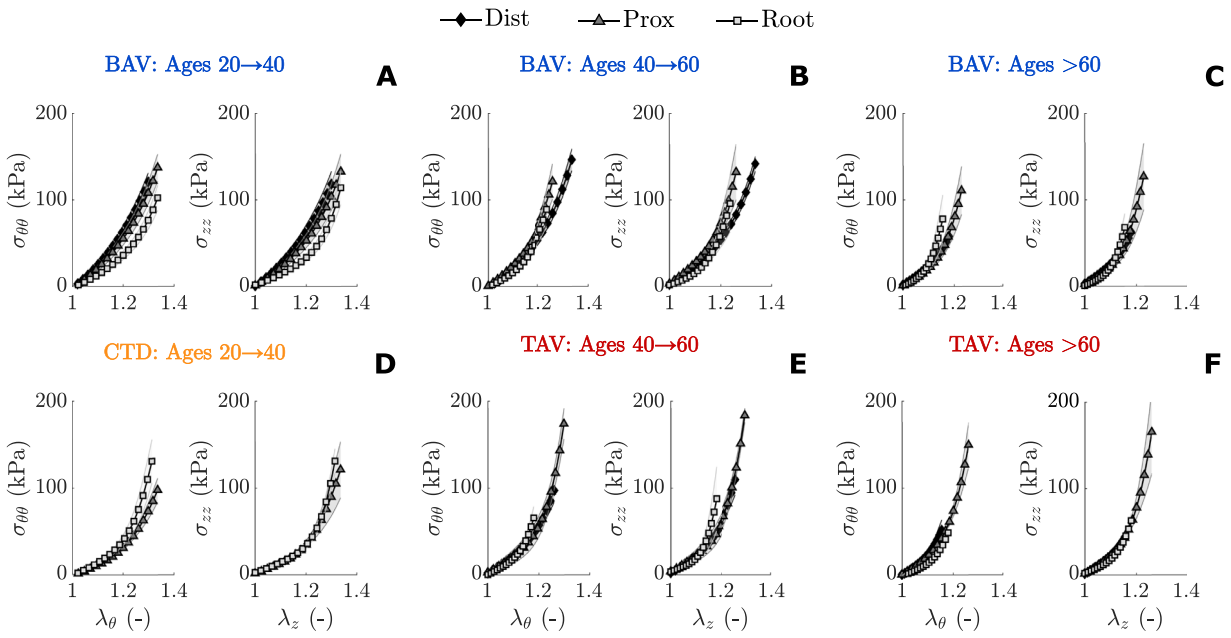

Fig. 1. Regional variation in representative equibiaxial Cauchy stress (σ) vs. stretch (λ) responses of ATAA tissues organized by etiology and age. Root, proximal, and distal behavior from young (**A**), middle-aged (**B**), and older (**C**) BAV patients. Root and proximal behavior from young (**D**) CTD patients. Root, proximal, and distal behavior from middle-aged (**E**) and older (**F**) TAV patients. Subscripts refer to circumferential (θ) and axial (z) directions. Individual data points are averages of interpolated equibiaxial responses across samples within each anatomical, chronological, and etiological group. Shaded areas visualize inter-specimen variability as ±SEM. The number of samples in each group is reported in Table S1. Average responses shown for groups with at least $n = 4$ samples.

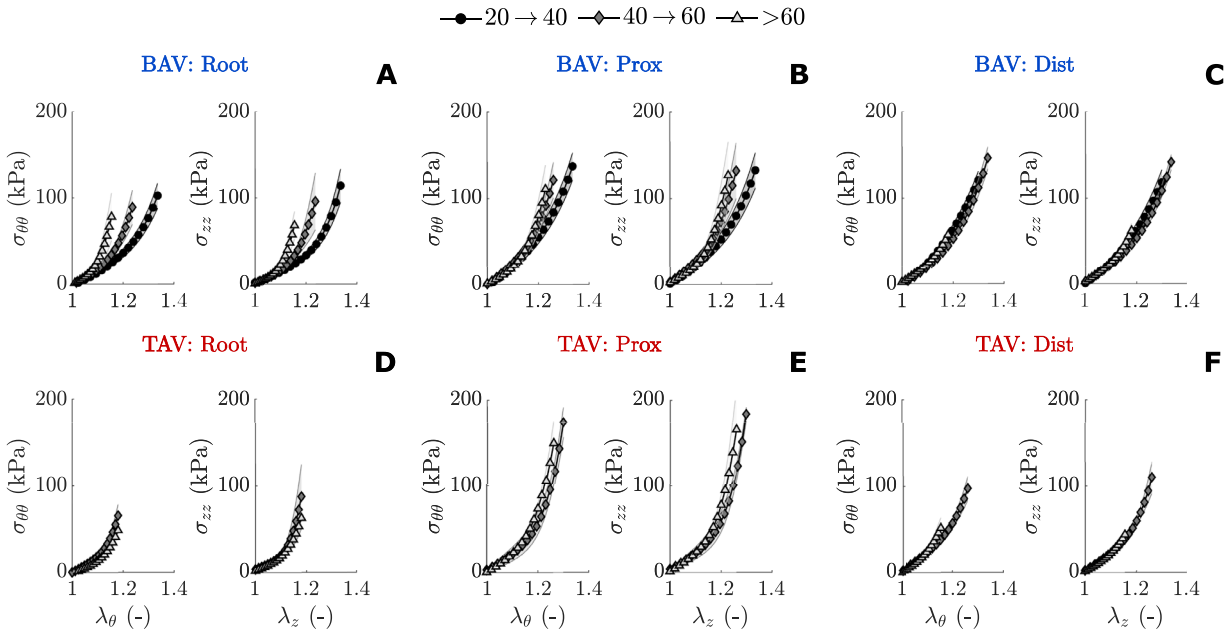

Fig. 2. Age-dependent variation in representative equibiaxial Cauchy stress (σ) vs. stretch (λ) responses of ATAA tissues organized by etiology and region. Root (**A**), proximal (**B**), and distal (**C**) behavior from young, middle-aged, and older BAV patients. Root (**D**), proximal (**E**), and distal (**F**) behavior from middle-aged and older TAV patients. Subscripts refer to circumferential (θ) and axial (z) directions. Individual data points are averages of interpolated equibiaxial responses across samples within each anatomical, chronological, and etiological group. Shaded areas visualize inter-specimen variability as ±SEM. The number of samples in each group is reported in Table S1. Average responses shown for groups with at least $n = 4$ samples.

the distal region (261±13 kPa) compared to both root (331±19 kPa; $p < 0.05$) and proximal (332±16 kPa; $p < 0.01$) segments (Fig. 4E). In contrast, no difference across regions surfaced in the axial stress (Fig. 4B). Nevertheless, the intrinsic stiffness of ATAA tissues progressively declined when moving distally from the heart, in both the axial (Root: 3.4±0.2 MPa, Prox: 2.9±0.2 MPa, Dist: 2.3±0.1 MPa; $p < 0.01$ or $p < 0.05$; Fig. 4C) and circumferential (Root: 5.8±0.3 MPa, Prox: 4.0±0.3 MPa, Dist: 2.8±0.3 MPa; $p < 0.01$ or $p < 0.05$; Fig. 4F) directions. Finally, the root stored less elastic energy (35±4 kPa) than more distal regions of ATAA samples, though only significantly so when compared to the proximal segment (52±5 kPa; $p < 0.01$; Fig. 4I).

Given the inherent regional differences in the biaxial mechanics of ATAA tissues, we evaluated the contribution of additional risk factors, i.e., older age, valve morphology, and the presence of a connective tissue disorder, within each anatomical segment.

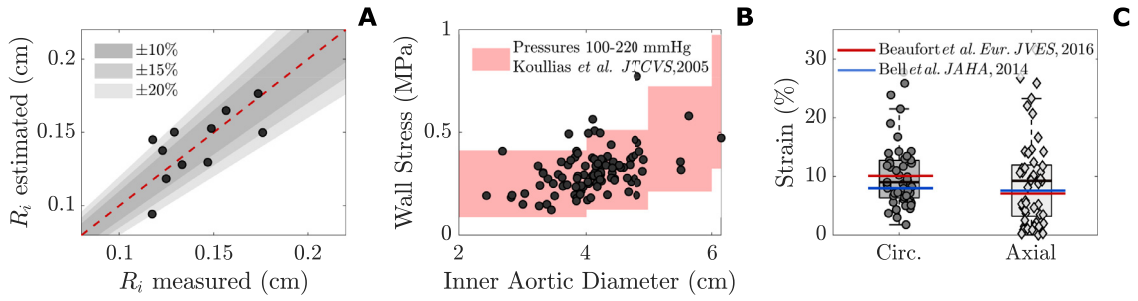

Fig. 3. Comparison of model predictions against independent experimental measurements of unloaded dimensions and reported levels of *in-vivo* circumferential stress or cyclic biaxial strains in patients suffering from ATAA disease. Estimates of unloaded inner radius (R_i) deviate by at most ±20% from intra-operative measurements on excised ATAA samples (**A**). Through-thickness integral mean of circumferential Cauchy stress at systolic pressure and crossover axial stretch fall within the reported range for ATAA patients [51] (**B**). Estimates of diastolic axial stretch yield cyclic circumferential and axial strains that are comparable to imaging-based measurements in patients with proximal and/or distal ATAA disease [52] and in older but non-aneurysmal individuals [53] (**C**).

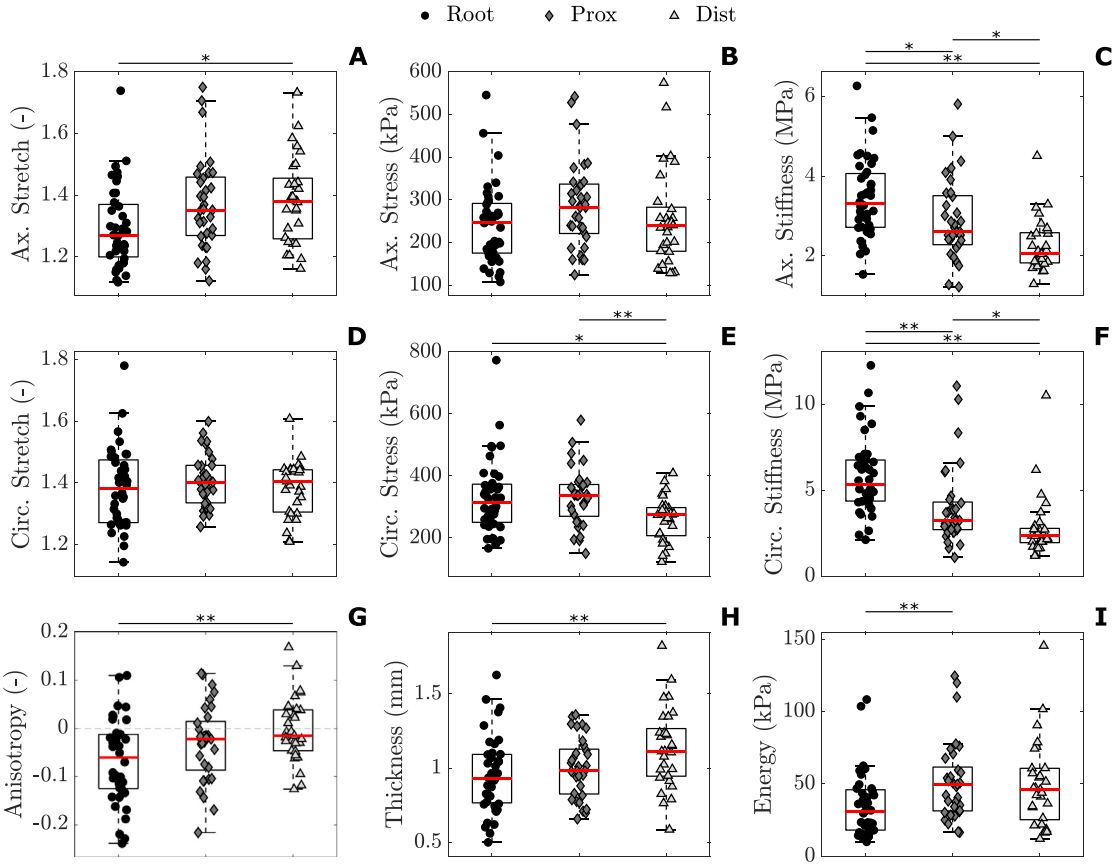

Fig. 4. Material, geometrical, and structural properties of root, proximal, and distal segments of ATAA samples within our patient cohort. Metrics of stress (**B, E**), stiffness (**C, F**), anisotropy (**G**), thickness (**H**), and stored energy (**I**) are calculated at estimated crossover axial stretch (**A**) and circumferential stretch (**D**) to accommodate systolic pressure. Note the gradual decline in biaxial tissue stiffness with increasing distance from the heart. Statistical significance between regions denoted by overbar, with * for $p < 0.05$ and ** for $p < 0.01$.

As expected from the qualitative comparison of average equibiaxial responses (Fig. 2), systolic deformation gradually decreased with advancing age in both the axial (Root: 1.39 → 1.20, r_s=-0.672, $p < 0.01$; Prox: 1.49 → 1.28, r_s=-0.496, $p < 0.01$; Dist: 1.59 → 1.27, r_s=-0.816, $p < 0.01$; Fig. 5A) and circumferential (Root: 1.48 → 1.30, r_s=-0.650, $p < 0.01$; Prox: 1.47 → 1.36, r_s=-0.509, $p < 0.01$; Dist: 1.45 → 1.33, r_s=-0.530, $p < 0.01$; Fig. 5D) directions. The age-induced decline of the axial stretch outpaced that of the circumferential stretch in distal tissues, where anisotropy progressively shifted from positive to negative (Dist: 0.09 → -0.04, r_s=-0.678, $p < 0.01$; Fig. 5G). Wall thickness increased with advancing age across all regions of ATAA samples (Root: 0.78 → 1.07, r_s=0.630, $p < 0.01$; Prox: 0.88 → 1.09, r_s=0.401, $p < 0.05$; Dist: 0.82 → 1.30, r_s=0.659, $p < 0.01$; Fig. 5H). Concurrently, circumferential stress at the root (Root: 404 → 287 kPa, r_s=-0.512, $p < 0.01$; Fig. 5E) and axial stress at the root and in the distal segment of ATAA samples (Root: 304 → 197 kPa, r_s=-0.525, $p < 0.01$; Dist: 423 → 190 kPa, r_s=-0.720, $p < 0.01$; Fig. 5B) decreased as patients became older. Advancing age correlated with circumferential stiffening in the proximal and distal ATAA tissues (Prox: 3.2 → 5.1 MPa, r_s=0.344, $p < 0.05$; Dist: 1.8 → 3.8 MPa, r_s=0.536, $p < 0.01$; Fig. 5F), yet it did not affect axial stiffness at any anatomical location (Fig. 5C). Related to decreased deformation, energy storage in ATAA tissues gradually declined with age in all segments (Root: 52 → 21 kPa, r_s=-0.683, $p <$

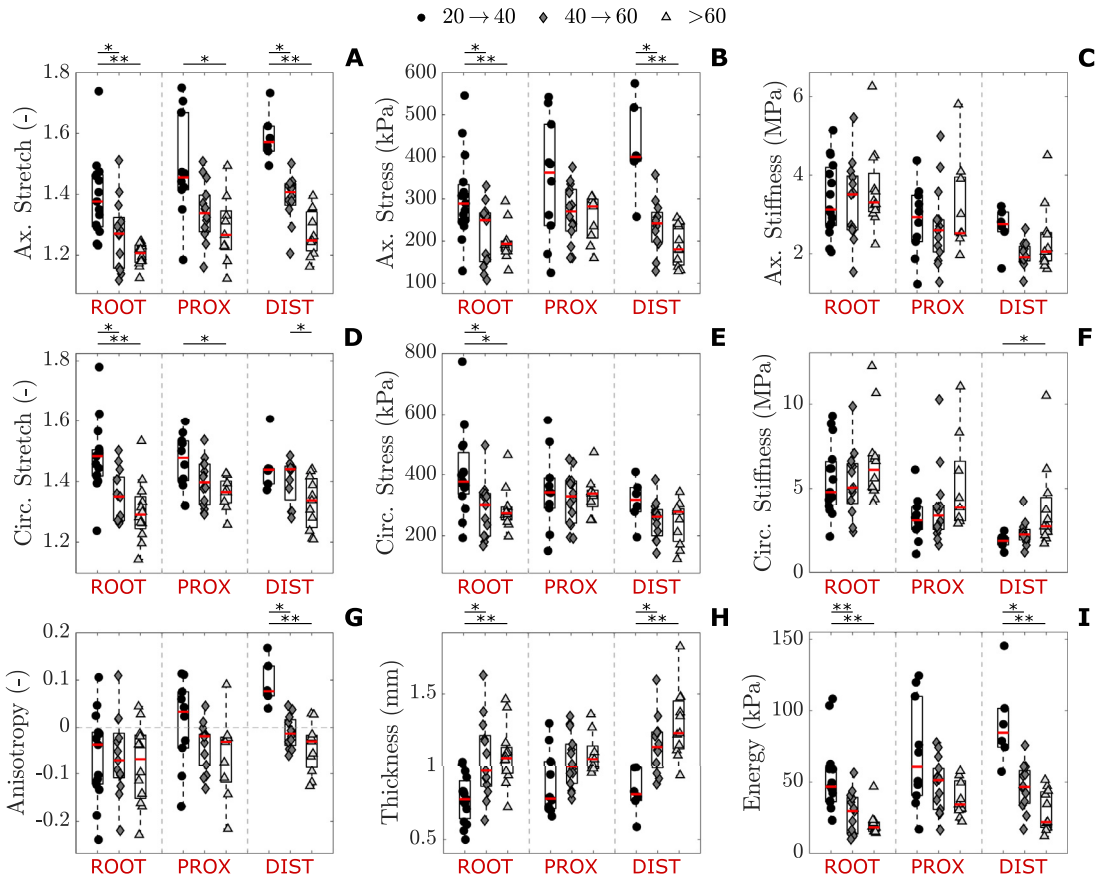

Fig. 5. Material, geometrical, and structural properties of root, proximal, and distal regions of ATAA samples from young, middle-age, and older patients enrolled in our study. Metrics of stress (**B, E**), stiffness (**C, F**), anisotropy (**G**), thickness (**H**), and stored energy (**I**) are calculated at estimated crossover axial stretch (**A**) and circumferential stretch (**D**) to accommodate systolic pressure. Note the negative correlation between advancing age and aortic function (through energy storage) across all three segments of ATAA samples. Statistical significance between age groups denoted by overbar, with * for $p < 0.05$ and ** for $p < 0.01$.

0.01; Prox: 69 → 38 kPa, r_s=-0.364, $p < 0.05$; Dist: 91 → 30 kPa, r_s=-0.746, $p < 0.01$; Fig. 5I). Plots of all mechanical metrics against age are included in the Supplementary Material (Figs. S5-7).

Etiological differences in the mechanics of ATAA tissues primarily emerged within the distal segment, where a thicker wall (Fig. 6H) complemented lower biaxial stretches (Fig. 6A,D), axial stress (Fig. 6B), and energy storage (Fig. 6I) in TAV patients compared with either or both the BAV and CTD cohorts. The proximal region featured similar discrepancies across etiological groups but limited to circumferential stretch (Fig. 6D), axial stress (Fig. 6B), and energy storage (Fig. 6I). Aorthopaties related to BAV or CTD did not affect anisotropy (Fig. 6G), circumferential stress (Fig. 6E), or biaxial tissue stiffness (Fig. 6C,F) in proximal and distal tissues, nor any of the mechanical metrics at the root.

4. Discussion

Properly timed monitoring and treatment of aortic aneurysms is crucial for reducing the risk of premature death due to fatal dissection and/or rupture [2,3,54]. While endovascular repair has become a valuable option for the treatment of non-ruptured aneurysms in the abdominal and descending thoracic segments of the aorta, it has only been performed on ascending thoracic aortic aneurysm (ATAA) patients that are ineligible for open surgical repair, using either commercial devices off-label or investigational devices [21,55]. Survival data from these studies show that patients with root disease experience worse outcomes than those with either proximal or distal disease [21]. Therefore, elucidating the uniqueness of the root in terms of structure, hemodynamics, and wall mechanics is imperative for the design of endovascular devices that can support the long-term survival of ATAA patients. To this end, we developed a methodological framework aimed to assess markers of lengthwise regional biomechanical dysfunction associated with ATAA disease.

We first sought to determine the representative (average) biaxial behavior of ATAA tissues as a function of region, age, and etiology. While our testing approach maximized the data yield by cycling a set of biaxial protocols through progressively higher stretch levels [56], it also increased inter-sample variability in the range of applied local strains. To circumvent this issue, previous studies have leveraged constitutive modeling to simulate consistent planar biaxial data [18]. As an alternative approach, we showed here that biquintic Hermite surfaces [38,41] faithfully capture the stress-strain behavior of ATAA tissues (average goodness of fit R^2=0.9846) and support direct interpolation of standard biaxial responses suitable for averaging (Fig. S1B). Besides facilitating qualitative cross-group comparisons [40,57], average data supply representative constitutive descriptors for complementary finite element analysis (Table S1) [58,59]. Notwithstanding these advantages, surface fitting limits the average behavior up to the maximum strain experienced by the least-stretched sample. This is particularly evident in the distal region, where a significant number of tissue specimens exhibited fairly linear stress-strain responses due to sub optimal loading that failed to engage collagen fibers (Fig. 2C). We thus recommend that more data be collected to capture the full scope of the tissue behavior in this ATAA segment.

Paralleling findings for aneurysmal tissues in the abdominal aorta [60], the average equibiaxial Cauchy stress vs. stretch

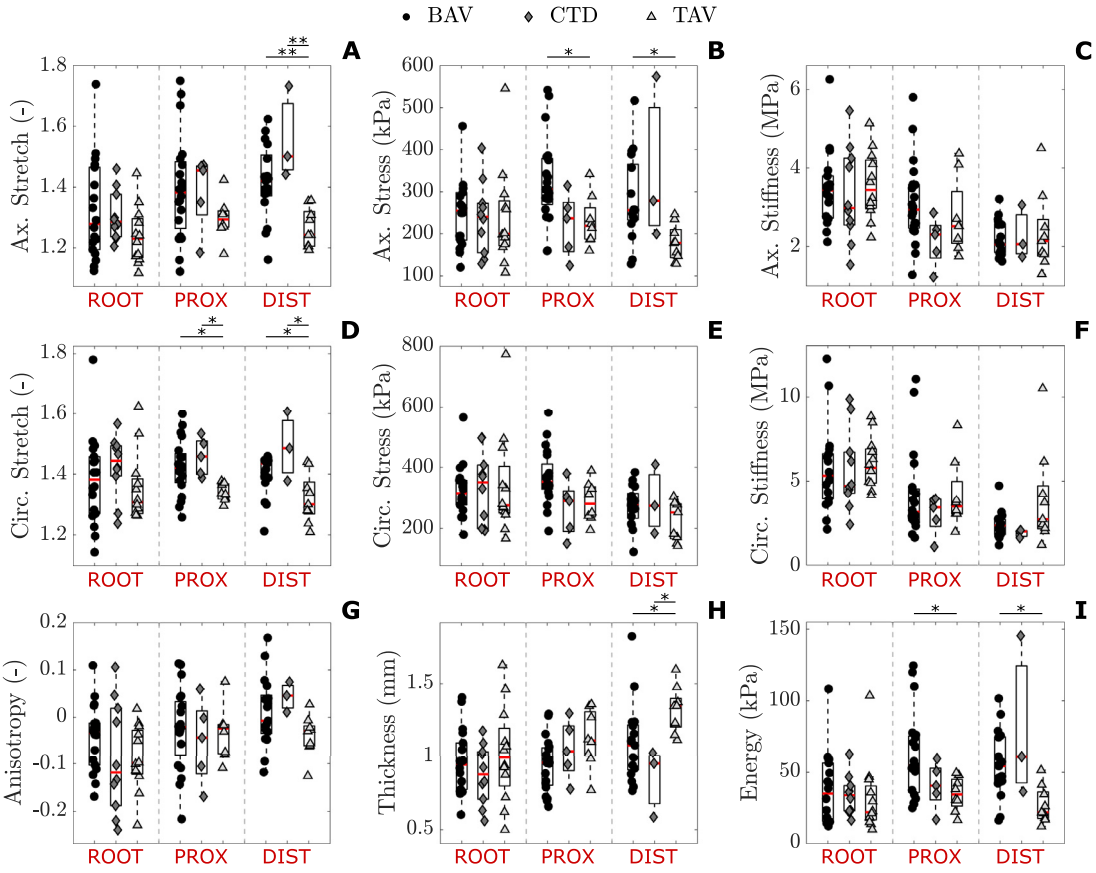

Fig. 6. Material, geometrical, and structural properties of root, proximal, and distal regions of ATAA samples from BAV, CTD, and TAV patients enrolled in our study. Metrics of stress (**B, E**), stiffness (**C, F**), anisotropy (**G**), thickness (**H**), and stored energy (**I**) are calculated at estimated crossover axial stretch (**A**) and circumferential stretch (**D**) to accommodate systolic pressure. Note the absence of consistent etiological differences across the three segments of ATAA samples. Statistical significance between etiological groups denoted by overbar, with * for $p < 0.05$ and ** for $p < 0.01$.

response in the low stiffness region of ATAA samples is qualitatively similar across all but young bicuspid aortic valve (BAV) patients, yet aging and proximity to the left ventricle anticipate the transition toward rapid strain-stiffening (Figs. 1,2). The trend toward reduced equibiaxial transition stretches that manifests in healthy human aortic tissues with advancing age [18] therefore persists with aneurysmal disease and is most prominent in the BAV cohort, due to the wider range of patient ages and the larger number of samples in this group. Earlier equibiaxial transition stretches at the root vs. more distal regions of ATAA [61] samples further mirror the behavior of the aortic sinus compared to the ascending aorta in healthy pigs [62] and humans [63]. Note, delayed transition and reduced stress at low-stiffness in root samples from BAV patients under 40 years-of-age (Fig. 1A) may indicate more severe microstructural disarray [64] compared to proximal and distal tissues and should be investigated by histological analysis.

Given the nonlinear response of ATAA tissues (Fig. S1B), mechanical metrics of stress, intrinsic stiffness, and elastic strain energy vary with the deformation. To determine the circumferential stretch compatible with patient-specific measures of traction-free wall thickness and systolic luminal diameter, we solved equilibrium equations for inflation-extension kinematics, constraining the axial stretch to fulfill the energetically-optimal, crossover condition that characterizes the axial force *vs.* length relationship for arterial samples (Fig. S1C) [65]. Minimization of modeling assumptions through incorporation of *in-vivo* data facilitated prediction of deformation-dependent mechanical metrics at patient- and region-specific biaxial stretches, permissive of more relevant and fair comparisons across groups (Figs. 4–6). In contrast, previous studies extracted either peak stretch/stress, tangential stiffness, or energy loss from either experimental [16,32,63,66] or simulated equibiaxial responses [25], when the axial and circumferential directions experience the same loading conditions. The anisotropy of aneurysmal tissues and the high degree of variability in the mechanical response across samples (Figs. 1,2) render these circumstances unlikely to hold *in-vivo*, further emphasizing the value of our multi-modal analysis for quantifying biaxial deformations. Although frequently used to probe cardiovascular tissue mechanics, *in-vivo* imaging [23,67–69] and *in-vitro* testing [14,16,24,25,32,63] individually offer limited capabilities [70]. We showed here that coupling of data from both testing modalities with mechanical models of the aortic wall supports inferences of mechanical metrics at consistent and physiologically-meaningful levels of deformation (Fig. 3). Note, however, that in adult wild-type mice the systolic axial stretch of the ascending thoracic aorta extends to at most 85% of the crossover value, thereby suggesting the presence of an exertion reserve for supplementing elastic energy between rest and strenuous exercise, emotional distress, or fight/flight conditions [71]. Therefore, by selecting the crossover axial stretch, our model provides the upper bound of tissue stress, stiffness, and energy, especially considering that *in-vivo* pressure and luminal diameter were measured under anesthesia. Indeed, the through-thickness integral mean of circumferential stress approached values reported for ATAA tissues at 220 mmHg pressure load [51], despite the average systolic pressure in our population not exceeding 150 mmHg (Fig. 3B). Further inaccuracies may

have been introduced by using a cylindrical geometry assumption in the predictions of the mechanics for non-axisymmetric ATAAs.

In agreement with the global trend that emerged from the comparison of averaged equibiaxial data (Fig. 1), biaxial tissue stiffness under simulated inflation-extension kinematics at patient-specific systolic pressure is largest at the ATAA root and decreases toward the proximal and distal segments (Fig. 4C,F). The axial gradient in tissue stiffness along ATAA samples complements evidence of circumferential heterogeneity reported in previous studies [25,72] and upholds the rapid stiffening of the aortic sinus compared to the rest of the non-aneurysmal ascending aorta from both porcine [62] and human cadaver [63] donors. Note, we have recently shown that circumferential tissue stiffness correlates with disease severity across mouse models of thoracic aortic aneurysm [73]. Stiffening of aneurysmal tissues is attributed to an earlier engagement of collagen fibers to compensate for the loss of integrity in the elastic laminae [74]. Interestingly, the elastic fiber network is looser and the collagen fibers are more haphazardly distributed at the root of the non-aneurysmal ascending aorta, compared to the proximal and distal regions [63]. Therefore, the inherent microstructure of the root may precipitate tissue stiffening in aneurysmal disease and synergize with increased procedural difficulty to worsen the outcomes of endovascular repair for this aortic segment [21]. Finally, root aneurysms have stronger genetic etiology, while proximal and distal disease is primarily linked to hemodynamics, particularly in BAV patients [75]. Overall, the structural, mechanical, and etiological gradients along ATAA samples urge for region-specific surgical interventions. We speculate that an adaptive design accounting for the intrinsic stiffness of the landing zone may help minimize the mechanical mismatch between stent-graft and aneurysmal tissues, reducing complications that could lead to poor surgical outcomes, particularly in the treatment of root disease [21].

The spatial gradient in circumferential tissue stiffness along ATAA samples persists when patients are grouped by age (Fig. 5F). A reflection of the positive correlation between aging and the circumferential stiffening of root, proximal, and distal tissues, this finding corroborates previous observations in both control [17–19] and aneurysmal [72,76] samples. The age-dependent decline in biaxial stretches under systolic pressure load (Fig. 5A,D) further mirrors the lower crossover axial stretch of the non-aneurysmal descending thoracic aorta of older patients [19] and contributes to reducing the elastic energy available for diastolic blood flow augmentation (Fig. 5I). Decreased stored energy hinders the aged ATAA wall from acting as a pressure reservoir and may increase the workload on the heart or damage the microvasculature [77,78]. Loss of elastic fiber integrity and deposition of collagen with both aging and aneurysmal disease [64,79,80] likely contribute to reducing the elastic energy storage within the aortic wall [74,81,82]. Overall, age emerges as the strongest predictor of tissue mechanics within our patient cohort.

Since ATAA disease is age-selective by etiology (Table 1), the reported divergence in mechanical descriptors between tricuspid aortic valve patients (TAV) and BAV [11–13,83–86] or syndromic aneurysm (CTD) [14–16] cohorts may depend, at least in part, on the age at which the disease typically manifests in these etiological groups. For instance, tissues from TAV patients enrolled in our study are thicker (Fig. 6H), operate at lower stretches (Fig. 6A,D), and store less elastic energy (Fig. 6I) compared to tissues in the BAV group, yet these differences are consistent with the average older age of TAV patients (Figs. S5–7). Aligned with this interpretation, Okamoto et al. showed that age influences the mechanical properties of aneurysmal ascending aortas, regardless of the underlying source of dilatation [14]. Recognizing the age discrepancy across etiologies, Sulejmani et al. limited the comparison between Marfan and non-Marfan thoracic aneurysmal tissues to patients above 40 years-of-age and noted larger equibiaxial transition strains in the Marfan group, though only significantly so in the circumferential direction [16]. This finding mirrors the delayed stiffening of the average equibiaxial responses in root tissues from CTD compared to TAV patients in our middle age cohort (Fig. S3C) and may reflect an abundance of thinner and loosely-packed collagen fibers with reduced load bearing capability [16]. Nevertheless, differences between CTD and TAV tissues fade when mechanical metrics are evaluated at patient-specific systolic pressure and crossover axial stretch within the same age group (Figs. S5–7). Leveraging finite element simulations, Xuan et al. further reported that tissues from the aortic sinuses experience larger circumferential stress compared to the sinotubular junction in Marfan patients alone [87], emphasizing the influence of axial location on mechanics (Fig. 4) and the perniciousness of root aortopathies associated with connective tissue disorders.

4.1. Conclusions

In response to the clinical need for alternative treatment options beyond open surgical repair, detailed characterization of the lengthwise regional mechanics of ATAA tissues offers invaluable guidance in formulating design specifications and testing parameters for the development and regulatory evaluation of endovascular devices catered specifically to the ascending aorta. Leveraging a multidisciplinary approach at the interface between clinical sciences and engineering, we coupled semi-inverse constitutive and forward modeling with *in-vitro* biaxial data and *in-vivo* blood pressure and diameter measurements to extract mechanical descriptors of aortic behavior at physiologically meaningful levels of deformation, while minimizing assumptions on tissue loading conditions. Our analysis revealed inherent axial regional differences in the biaxial mechanics of ATAA tissues across a diverse patient cohort, which persist with age and disease. Moving distally from the aortic root to the first ascending aortic branch, we observed an increase in crossover stretch, thickness, and energy storage, accompanied by a progressive decline in circumferential and axial stiffness. Furthermore, we showed that aging leads to reduced aortic function independent of anatomical location and is a stronger predictor of mechanical response than either valve morphology or underlying syndromic disorder. These findings further our current understanding of the regional biomechanical derangement in ATAA tissues and provide evidence to elucidate disease pathogenesis, predict lesion progression, and identify appropriate treatment course.

Declaration of Competing Interest

The Authors have nothing to declare.

Acknowledgments

This work was supported by the High-Risk Cardiovascular Research Philanthropy Fund, The Stephens Family Endowed Chair, Educational Grants from Cook Medical, CryoLife, Gore Medical, Medtronic, and Terumo Aortic (to EER), NIH/NHLBI – UM1HL088955 (supporting BK as Clinical Research Scholar of the Cardiothoracic Surgical Trials Network), and NSF CAREER 2049088 (to RA).

Supplementary material

Supplementary material associated with this article can be found, in the online version, at doi:10.1016/j.actbio.2023.03.023.

References

[1] G.A. Kuzmik, A.X. Sang, J.A. Elefteriades, Natural history of thoracic aortic aneurysms, J. Vasc. Surg. 56 (2) (2012) 565–571, doi:10.1016/j.jvs.2012.04.053.

[2] R. Gouveia, E. Melo, G.S. Duarte, A. Lopes, M. Alves, D. Caldeira, R. Fernandes, E. Fernandes, L.M. Pedro, Incidence and prevalence of thoracic aortic aneurysms: a systematic review and meta-analysis of population-based studies, Semin. Thoracic Cardiovasc. Surg. (2021) 3, doi:10.1053/j.semtcvs.2021.02.029.

[3] A. Pinard, G.T. Jones, D.M. Milewicz, Genetics of thoracic and abdominal aortic diseases, Circ. Res. 124 (4) (2019) 588–606, doi:10.1161/CIRCRESAHA.118.312436.

[4] N.P. Ostberg, M.A. Zafar, B.A. Ziganshin, J.A. Elefteriades, The genetics of thoracic aortic aneurysms and dissection: a clinical perspective, Biomolecules 10 (2) (2020) 1, doi:10.3390/biom10020182.

[5] H.C. Dietz, G.R. Cutting, R.E. Pyeritz, C.L. Maslen, L.Y. Sakai, G.M. Corson, E.G. Puffenberger, A. Hamosh, E.J. Nanthakumar, S.M. Curristin, Marfan syndrome caused by a recurrent de novo missense mutation in the fibrillin gene, Nature 352 (6333) (1991) 337–339, doi:10.1038/352337a0.

[6] G. Albornoz, M.A. Coady, M. Roberts, R.R. Davies, M. Tranquilli, J.A. Rizzo, J.A. Elefteriades, Familial thoracic aortic aneurysms and dissections-incidence, modes of inheritance, and phenotypic patterns, Ann. Thoracic Surg. 82 (4) (2006) 1400–1405, doi:10.1016/j.athoracsur.2006.04.098.

[7] B.L. Loeys, U. Schwarze, T. Holm, B.L. Callewaert, G.H. Thomas, H. Pannu, J.F. De Backer, G.L. Oswald, S. Symoens, S. Manouvrier, A.E. Roberts, F. Faravelli, M.A. Greco, R.E. Pyeritz, D.M. Milewicz, P.J. Coucke, D.E. Cameron, A.C. Braverman, P.H. Byers, A.M. De Paepe, H.C. Dietz, Aneurysm syndromes caused by mutations in the TGF-β receptor, N. Engl. J. Med. 355 (8) (2006) 788–798, doi:10.1056/NEJMoa055695.

[8] E.M. Isselbacher, Thoracic and abdominal aortic aneurysms, Circulation 111 (6) (2005) 816–828, doi:10.1161/01.CIR.0000154569.08857.7A.

[9] S. Verma, S.C. Siu, Aortic dilatation in patients with bicuspid aortic valve, N. Engl. J. Med. 370 (20) (2014) 1920–1929, doi:10.1056/NEJMra1207059.

[10] S. Pasta, J.A. Phillippi, T.G. Gleason, D.A. Vorp, Effect of aneurysm on the mechanical dissection properties of the human ascending thoracic aorta, J. Thoracic Cardiovasc. Surg. 143 (2) (2012) 460–467, doi:10.1016/j.jtcvs.2011.07.058.

[11] C. Forsell, H.M. Björck, P. Eriksson, A. Franco-Cereceda, T.C. Gasser, Biomechanical properties of the thoracic aneurysmal wall: differences between bicuspid aortic valve and tricuspid aortic valve patients, Ann. Thoracic Surg. 98 (1) (2014) 65–71, doi:10.1016/j.athoracsur.2014.04.042.

[12] A. Ferrara, P. Totaro, S. Morganti, F. Auricchio, Effects of clinico-pathological risk factors on in-vitro mechanical properties of human dilated ascending aorta, J. Mech. Behav. Biomed.Mater. 77 (2018) 1–11, doi:10.1016/j.jmbbm.2017.08.032.

[13] J.C.-Y. Chung, E. Wong, M. Tang, D. Eliathamby, T.L. Forbes, J. Butany, C.A. Simmons, M. Ouzounian, Biomechanics of aortic dissection: a comparison of aortas associated with bicuspid and tricuspid aortic valves, J. Am. Heart Assoc. 9 (15) (2020), doi:10.1161/JAHA.120.016715. E016715–e016715

[14] R.J. Okamoto, J.E. Wagenseil, W.R. DeLong, S.J. Peterson, N.T. Kouchoukos, T.M.R. Sundt, Mechanical properties of dilated human ascending aorta, Ann. Biomed. Eng. 30 (5) (2002) 624–635.

[15] A. Jarrahi, A. Karimi, M. Navidbakhsh, H. Ahmadi, Experimental/numerical study to assess mechanical properties of healthy and marfan syndrome ascending thoracic aorta under axial and circumferential loading, Mater. Technol. 31 (5) (2016) 247–254, doi:10.1179/1753555715Y.0000000049.

[16] F. Sulejmani, A. Pokutta-Paskaleva, B. Ziganshin, B. Leshnower, G. Iannucci, J. Elefteriades, W. Sun, Biomechanical properties of the thoracic aorta in marfan patients, Ann. Cardiothorac. Surg. 6 (6) (2017) 610–624, doi:10.21037/acs.2017.09.12.

[17] D. Haskett, G. Johnson, A. Zhou, U. Utzinger, J.V. Geest, Microstructural and biomechanical alterations of the human aorta as a function of age and location, Biomech. Model. Mechanobiol. 9 (6) (2010) 725–736, doi:10.1007/s10237-010-0209-7.

[18] S. Roccabianca, C.A. Figueroa, G. Tellides, J.D. Humphrey, Quantification of regional differences in aortic stiffness in the aging human, J. Mech. Behav. Biomed.Mater. 29 (2014) 618–634, doi:10.1016/j.jmbbm.2013.01.026.

[19] M. Jadidi, M. Habibnezhad, E. Anttila, K. Maleckis, A. Desyatova, J. MacTaggart, A. Kamenskiy, Mechanical and structural changes in human thoracic aortas with age, Acta Biomater. 103 (2020) 172–188, doi:10.1016/j.actbio.2019.12.024.

[20] S. Trimarchi, C.A. Nienaber, V. Rampoldi, T. Myrmel, T. Suzuki, R.H. Mehta, E. Bossone, J.V. Cooper, D.E. Smith, L. Menicanti, A. Frigiola, J.K. Oh, M.G. Deeb, E.M. Isselbacher, K.A. Eagle, Contemporary results of surgery in acute type a aortic dissection: the international registry of acute aortic dissection experience, J. Thoracic Cardiovasc. Surg. 129 (1) (2005) 112–122, doi:10.1016/j.jtcvs.2004.09.005.

[21] E.E. Roselli, J.J. Idrees, D.R. Johnston, M.J. Eagleton, M.Y. Desai, L.G. Svensson, Zone zero thoracic endovascular aortic repair: a proposed modification to the classification of landing zones, J. Thoracic Cardiovasc. Surg. 155 (4) (2018) 1381–1389, doi:10.1016/j.jtcvs.2017.11.054.

[22] M.F. Fillinger, R.K. Greenberg, J.F. McKinsey, E.L. Chaikof, Reporting standards for thoracic endovascular aortic repair (TEVAR), J. Vasc. Surg. 52 (4) (2010) 1022–1033, doi:10.1016/j.jvs.2010.07.008.

[23] M. Alreshidan, N. Shahmansouri, J. Chung, V. Lash, A. Emmott, R.L. Leask, K. Lachapelle, Obtaining the biomechanical behavior of ascending aortic aneurysm via the use of novel speckle tracking echocardiography, J. Thoracic Cardiovasc. Surg. 153 (4) (2017) 781–788, doi:10.1016/j.jtcvs.2016.11.056.

[24] J. Chung, K. Lachapelle, R. Cartier, R. Mongrain, R.L. Leask, Loss of mechanical directional dependency of the ascending aorta with severe medial degeneration, Cardiovas. Pathol. 26 (2017) 45–50, doi:10.1016/j.carpath.2016.11.001.

[25] T. Sigaeva, S. Sattari, S. Polzer, J.J. Appoo, E.S.D. Martino, Biomechanical properties of ascending aortic aneurysms: quantification of inter- and intra-patient variability, J. Biomech. 125 (2021) 110542, doi:10.1016/j.jbiomech.2021.110542.

[26] E. Durbak, S. Tarraf, C. Gillespie, E. Germano, F. Cikach, E. Blackstone, K. Emerton, R. Colbrunn, C. Bellini, E.E. Roselli, Ex-vivo biaxial load testing analysis of aortic biomechanics demonstrates variation in elastic energy distribution across the aortic zone zero, J. Thoracic Cardiovasc. Surg. (2021), doi:10.1016/j.jtcvs.2021.09.071.

[27] H. Ince, C.A. Nienaber, Etiology, pathogenesis and management of thoracic aortic aneurysm, Nat. Clin. Pract. Cardiovasc. Med. 4 (8) (2007) 418–427, doi:10.1038/ncpcardio0937.

[28] M.R. Bersi, R. Khosravi, A.J. Wujciak, D.G. Harrison, J.D. Humphrey, Differential cell-matrix mechanoadaptations and inflammation drive regional propensities to aortic fibrosis, aneurysm or dissection in hypertension, J. R. Soc. Interface 14 (136) (2017) 11, doi:10.1098/rsif.2017.0327.

[29] B.D. Stemper, N. Yoganandan, M.R. Stineman, T.A. Gennarelli, J.L. Baisden, F.A. Pintar, Mechanics of fresh, refrigerated, and frozen arterial tissue, J. Surg. Res. 139 (2) (2007) 236–242, doi:10.1016/j.jss.2006.09.001.

[30] S.D. Salinas, M.M. Clark, R. Amini, The effects of -80C short-term storage on the mechanical response of tricuspid valve leaflets, J. Biomech. 98 (2020) 1, doi:10.1016/j.jbiomech.2019.109462.

[31] K.L. Billiar, M.S. Sacks, Biaxial mechanical properties of the natural and glutaraldehyde treated aortic valve cusp–Part I: experimental results, J. Biomech. Eng. 122 (1) (2000) 23–30.

[32] J.P.V. Geest, M.S. Sacks, D.A. Vorp, The effects of aneurysm on the biaxial mechanical behavior of human abdominal aorta, J. Biomech. 39 (7) (2006) 1324–1334, doi:10.1016/j.jbiomech.2005.03.003.

[33] A.V. Kamenskiy, Y.A. Dzenis, S.A. Kazmi, M.A. Pemberton, I.I. Pipinos, N.Y. Phillips, K. Herber, T. Woodford, R.E. Bowen, C.S. Lomneth, J.N. MacTaggart, Biaxial mechanical properties of the human thoracic and abdominal aorta, common carotid, subclavian, renal and common iliac arteries, Biomech. Model. Mechanobiol. 13 (6) (2014) 1341–1359, doi:10.1007/s10237-014-0576-6.

[34] B.C. Perez, J. Tang, H.J. Morris, J.R. Palko, X. Pan, R.T. Hart, J. Liu, Biaxial mechanical testing of posterior sclera using high-resolution ultrasound speckle tracking for strain measurements, J. Biomech. 47 (5) (2014) 1151–1156, doi:10.1016/j.jbiomech.2013.12.009.

[35] C.J. Ross, D.W. Laurence, A.L. Echols, A.R. Babu, T. Gu, G.A. Duginski, C.H. Johns, B.T. Mullins, K.M. Casey, K.A. Laurence, Y.D. Zhao, R. Amini, K.M. Fung, A. Mir, H.M. Burkhart, Y. Wu, G.A. Holzapfel, C.H. Lee, Effects of enzyme-based removal of collagen and elastin constituents on the biaxial mechanical responses of porcine atrioventricular heart valve anterior leaflets, Acta Biomater. 135 (2021) 425–440, doi:10.1016/j.actbio.2021.08.043.

[36] S.D. Salinas, Y.M. Farra, K.A. Khoiy, J. Houston, C.H. Lee, C. Bellini, R. Amini, The role of elastin on the mechanical properties of the anterior leaflet in porcine tricuspid valves, PLoS ONE 17 (2022) 5, doi:10.1371/journal.pone.0267131.

[37] K.A. Khoiy, A.D. Pant, R. Amini, Quantification of material constants for a phenomenological constitutive model of porcine tricuspid valve leaflets for simulation applications, J. Biomech. Eng. 140 (9) (2018) 5, doi:10.1115/1.4040126.

[38] D.B. Smith, M.S. Sacks, D.A. Vorp, M. Thornton, Surface geometric analysis of anatomic structures using biquintic finite element interpolation, Ann. Biomed. Eng. 28 (6) (2000) 598–611, doi:10.1114/1.1306342.

[39] W.R. Barone, R. Amini, S. Maiti, P.A. Moalli, S.D. Abramowitch, The impact of boundary conditions on surface curvature of polypropylene mesh in response to uniaxial loading, J. Biomech. 48 (9) (2015) 1566–1574, doi:10.1016/j.jbiomech.2015.02.061.

[40] B. Fata, W. Zhang, R. Amini, M.S. Sacks, Insights into regional adaptations in the growing pulmonary artery using a meso-scale structural model: effects of ascending aorta impingement, J. Biomech. Eng. 136 (2) (2014) 21009, doi:10.1115/1.4026457.

[41] C.P. Bradley, A.J. Pullan, P.J. Hunter, Geometric modeling of the human torso using cubic hermite elements, Ann. Biomed. Eng. 25 (1) (1997) 96–111, doi:10.1007/BF02738542.

[42] C.E. Eckert, B. Zubiate, M. Vergnat, J.H. Gorman, R.C. Gorman, M.S. Sacks, In vivo dynamic deformation of the mitral valve annulus, Ann. Biomed. Eng. 37 (9) (2009) 1757–1771, doi:10.1007/s10439-009-9749-3.

[43] R. Amini, C.E. Eckert, K. Koomalsingh, J. McGarvey, M. Minakawa, J.H. Gorman, R.C. Gorman, M.S. Sacks, On the in vivo deformation of the mitral valve anterior leaflet: effects of annular geometry and referential configuration, Ann. Biomed. Eng. 40 (7) (2012) 1455–1467, doi:10.1007/s10439-012-0524-5.

[44] C. Bellini, P. Glass, M. Sitti, E.S.D. Martino, Biaxial mechanical modeling of the small intestine, J. Mech. Behav. Biomed.Mater. 4 (8) (2011) 1727–1740, doi:10.1016/j.jmbbm.2011.05.030.

[45] C. Bellini, E.S.D. Martino, A mechanical characterization of the porcine atria at the healthy stage and after ventricular tachypacing, J. Biomech. Eng. 134 (2) (2012) 21008, doi:10.1115/1.4006026.

[46] C. Bellini, E.S.D. Martino, S. Federico, Mechanical behaviour of the human atria, Ann. Biomed. Eng. 41 (7) (2013) 1478–1490, doi:10.1007/s10439-012-0699-9.

[47] S. Federico, A. Grillo, G. Giaquinta, W. Herzog, Convex Fung-type potentials for biological tissues, Meccanica 43 (3) (2008) 279–288, doi:10.1007/s11012-007-9090-6.

[48] A.N. Azadani, S. Chitsaz, A. Mannion, A. Mookhoek, A. Wisneski, J.M. Guccione, M.D. Hope, L. Ge, E.E. Tseng, Biomechanical properties of human ascending thoracic aortic aneurysms, Ann. Thoracic Surg. 96 (1) (2013) 50–58, doi:10.1016/j.athoracsur.2013.03.094.
[49] H.W. Weizsäcker, H. Lambert, K. Pascale, Analysis of the passive mechanical properties of rat carotid arteries, J. Biomech. 16 (9) (1983) 703–715, doi:10.1016/0021-9290(83)90080-5.
[50] S. Baek, R.L. Gleason, K.R. Rajagopal, J.D. Humphrey, Theory of small on large: potential utility in computations of fluid-solid interactions in arteries, Comput. Methods Appl. Mech.Eng. 196 (31) (2007) 3070–3078, doi:10.1016/j.cma.2006.06.018.
[51] G. Koullias, R. Modak, M. Tranquilli, D.P. Korkolis, P. Barash, J.A. Elefteriades, Mechanical deterioration underlies malignant behavior of aneurysmal human ascending aorta, J. Thoracic Cardiovasc. Surg. 130 (3) (2005) 677–683, doi:10.1016/j.jtcvs.2005.02.052.
[52] H.W.L. de Beaufort, F.J.H. Nauta, M. Conti, E. Cellitti, C. Trentin, E. Faggiano, G.H.W. van Bogerijen, C.A. Figueroa, F.L. Moll, J.A. van Herwaarden, F. Auricchio, S. Trimarchi, Extensibility and distensibility of the thoracic aorta in patients with aneurysm, Eur. J. Vasc. Endovasc.Surg. 53 (2) (2017) 199–205, doi:10.1016/j.ejvs.2016.11.018.
[53] V. Bell, W.A. Mitchell, S. Sigurðsson, J.J.M. Westenberg, J.D. Gotal, A.A. Torjesen, T. Aspelund, L.J. Launer, A. de Roos, V. Gudnason, T.B. Harris, G.F. Mitchell, Longitudinal and circumferential strain of the proximal aorta, J. Am. Heart Assoc. 3 (6) (2014), doi:10.1161/JAHA.114.001536. E001536
[54] J.A. Elefteriades, J.A. Rizzo, Epidemiology, prevalence, incidence, trends, in: Acute Aortic Disease, Informa Healthcare, New York, NY, 2008, pp. 89–98.
[55] E.E. Roselli, J. Idrees, R.K. Greenberg, D.R. Johnston, B.W. Lytle, Endovascular stent grafting for ascending aorta repair in high-risk patients, J. Thoracic Cardiovasc. Surg. 149 (1) (2015) 144–151, doi:10.1016/j.jtcvs.2014.07.109.
[56] M. Jadidi, S.A. Razian, M. Habibnezhad, E. Anttila, A. Kamenskiy, Mechanical, structural, and physiologic differences in human elastic and muscular arteries of different ages: Comparison of the descending thoracic aorta to the superficial femoral artery, Acta Biomater. 119 (2021) 268–283, doi:10.1016/j.actbio.2020.10.035.
[57] A. Forneris, M. Nightingale, A. Ismaguilova, T. Sigaeva, L. Neave, A. Bromley, R.D. Moore, E.S.D. Martino, Heterogeneity of ex vivo and in vivo properties along the length of the abdominal aortic aneurysm, Appl. Sci. 11 (8) (2021), doi:10.3390/app11083485.
[58] Y. Xuan, Z. Wang, R. Liu, H. Haraldsson, M.D. Hope, D.A. Saloner, J.M. Guccione, L. Ge, E. Tseng, Wall stress on ascending thoracic aortic aneurysms with bicuspid compared with tricuspid aortic valve, J. Thoracic Cardiovasc. Surg. 156 (2) (2018) 492–500, doi:10.1016/j.jtcvs.2018.03.004.
[59] S. Avril, M.W. Gee, A. Hemmler, S. Rugonyi, Patient-specific computational modeling of endovascular aneurysm repair: State of the art and future directions, Int. J. Numer. MethodsBiomed. Eng. 37 (12) (2021) E3529, doi:10.1002/cnm.3529.
[60] J.A. Niestrawska, P. Regitnig, C. Viertler, T.U. Cohnert, A.R. Babu, G.A. Holzapfel, The role of tissue remodeling in mechanics and pathogenesis of abdominal aortic aneurysms, Acta Biomater. (2019) 2, doi:10.1016/j.actbio.2019.01.070.
[61] B. Kramer, M. Thompson, E. Vianna, S. Tarraf, A. Snyder, B. Gentle, C. Gillespie, E. Germano, F. Cikach, A. Pande, J. Hargrave, R. Colbrunn, C. Bellini, E.E. Roselli, Longitudinal versus circumferential biomechanical behavior of the aneurysmal ascending aorta, American Association for Thoracic Surgery 103rd Annual Meeting, 2023. [Submitted]
[62] N. Gundiah, P.B. Matthews, R. Karimi, A. Azadani, J. Guccione, T.S. Guy, D. Saloner, E.E. Tseng, Significant material property differences between the porcine ascending aorta and aortic sinuses, J. Heart Valve Disease 17 (6) (2008) 606–613.
[63] A.N. Azadani, S. Chitsaz, P.B. Matthews, N. Jaussaud, J. Leung, T. Tsinman, L. Ge, E.E. Tseng, Comparison of mechanical properties of human ascending aorta and aortic sinuses, Ann. Thoracic Surg. 93 (1) (2012) 87–94, doi:10.1016/j.athoracsur.2011.08.002.
[64] M. Nightingale, A. Gregory, T. Sigaeva, G.M. Dobson, P.W.M. Fedak, J.J. Appoo, E.S.D. Martino, Biomechanics in ascending aortic aneurysms correlate with tissue composition and strength, JTCVS Open 9 (2021) 1–10, doi:10.1016/j.xjon.2021.12.001.
[65] P.V. Loon, Length-force and volume-pressure relationships of arteries, Biorheology 14 (4) (1977) 181–201.
[66] J. Chung, K. Lachapelle, E. Wener, R. Cartier, B. De Varennes, R. Fraser, R.L. Leask, Energy loss, a novel biomechanical parameter, correlates with aortic aneurysm size and histopathologic findings, J. Thoracic Cardiovasc. Surg. 148 (3) (2014) 1082–1089, doi:10.1016/j.jtcvs.2014.06.021.
[67] R.K. Modak, G.J. Koullias, U.S. Govindarajulu, M. Tranquilli, P.G. Barash, J.A. Elefteriades, Ascending aortic aneurysms: asymmetrical differences in aortic cross-sectional wall motion detected by epiaortic echocardiography, J. Cardiothorac. Vasc. Anesth. 24 (5) (2010) 776–779, doi:10.1053/j.jvca.2010.03.012.
[68] N.P.E. Kadoglou, K.G. Moulakakis, I. Papadakis, I. Ikonomidis, M. Alepaki, A. Spathis, P. Karakitsos, J. Lekakis, C.D. Liapis, Differential effects of stent-graft fabrics on arterial stiffness in patients undergoing endovascular aneurysm repair, J. Endovasc. Ther. 21 (6) (2014) 850–858, doi:10.1583/14-4772MR.1.
[69] G. Andrea, R.-P. Jose, D.-S. Lydia, T.-T. Gisela, M. Giuliana, G. Laura, H. Marina, V. Filipa, G. Laura, G.-A. Teresa, J.K.M.W. Oliver, S.A. Augusto, G.-D. David, E. Arturo, Influence of aortic dilation on the regional aortic stiffness of bicuspid aortic valve assessed by 4-dimensional flow cardiac magnetic resonance, JACC Cardiovasc. Imaging 12 (6) (2019) 1020–1029, doi:10.1016/j.jcmg.2018.03.017.
[70] H.L. Cebull, V.L. Rayz, C.J. Goergen, Recent advances in biomechanical characterization of thoracic aortic aneurysms, Front. Cardiovasc. Med. 7 (2020) 75.
[71] J. Ferruzzi, P.D. Achille, G. Tellides, J.D. Humphrey, Combining in vivo and in vitro biomechanical data reveals key roles of perivascular tethering in central artery function, PLOS ONE 13 (9) (2018) E0201379.
[72] M.D. Giuseppe, G. Alotta, V. Agnese, D. Bellavia, G.M. Raffa, V. Vetri, M. Zingales, S. Pasta, M. Pilato, Identification of circumferential regional heterogeneity of ascending thoracic aneurysmal aorta by biaxial mechanical testing, J. Mol. Cell. Cardiol. 130 (2019) 205–215, doi:10.1016/j.yjmcc.2019.04.010.
[73] C. Bellini, M.R. Bersi, A.W. Caulk, J. Ferruzzi, D.M. Milewicz, F. Ramirez, D.B. Rifkin, G. Tellides, H. Yanagisawa, J.D. Humphrey, Comparison of 10 murine models reveals a distinct biomechanical phenotype in thoracic aortic aneurysms, J. R. Soc. Interface 14 (130) (2017) 5, doi:10.1098/rsif.2016.1036.
[74] C. Cavinato, M. Chen, D. Weiss, M.J. Ruiz-Rodríguez, M.A. Schwartz, J.D. Humphrey, Progressive microstructural deterioration dictates evolving biomechanical dysfunction in the marfan aorta, Front. Cardiovasc. Med. 8 (2021) 800730, doi:10.3389/fcvm.2021.800730.
[75] N.M. Yassine, J.T. Shahram, S.C. Body, Pathogenic mechanisms of bicuspid aortic valve aortopathy, Front. Physiol. 8 (2017) 687, doi:10.3389/fphys.2017.00687.
[76] A. Ferrara, S. Morganti, P. Totaro, A. Mazzola, F. Auricchio, Human dilated ascending aorta: Mechanical characterization via uniaxial tensile tests, J. Mech. Behav. Biomed.Mater. 53 (2016) 257–271, doi:10.1016/j.jmbbm.2015.08.021.
[77] M.F. O'Rourke, Arterial aging: pathophysiological principles, Vasc. Med. (London, England) 12 (4) (2007) 329–341, doi:10.1177/1358863X07083392.
[78] J. Ferruzzi, M.R. Bersi, S. Uman, H. Yanagisawa, J.D. Humphrey, Decreased elastic energy storage, not increased material stiffness, characterizes central artery dysfunction in fibulin-5 deficiency independent of sex, J. Biomech. Eng. 137 (3) (2015), doi:10.1115/1.4029431.
[79] A. Tsamis, J.T. Krawiec, D.A. Vorp, Elastin and collagen fibre microstructure of the human aorta in ageing and disease: a review, J. R. Soc. Interface 10 (83) (2013) 20121004, doi:10.1098/rsif.2012.1004.
[80] S. Yousef, N. Matsumoto, I. Dabe, M. Mori, A.B. Landry, S.-R. Lee, Y. Kawamura, C. Yang, G. Li, R. Assi, P. Vallabhajosyula, A. Geirsson, G. Moeckel, J.D. Humphrey, G. Tellides, Quantitative not qualitative histology differentiates aneurysmal from nondilated ascending aortas and reveals a net gain of medial components, Sci. Rep. 11 (1) (2021) 13185, doi:10.1038/s41598-021-92659-1.
[81] J. Ferruzzi, M.R. Bersi, R.P. Mecham, F. Ramirez, H. Yanagisawa, G. Tellides, J.D. Humphrey, Loss of elastic fiber integrity compromises common carotid artery function: implications for vascular aging, Artery Res. 14 (2016) 41–52, doi:10.1016/j.artres.2016.04.001.
[82] J.D. Humphrey, G. Tellides, Central artery stiffness and thoracic aortopathy, Am. J. Physiol. HeartCirc. Physiol. 316 (1) (2019) H169–H182, doi:10.1152/ajpheart.00205.2018.
[83] S. Albinsson, A.D. Corte, A. Alajbegovic, K.K. Krawczyk, C. Bancone, U. Galderisi, M. Cipollaro, M. De Feo, A. Forte, Patients with bicuspid and tricuspid aortic valve exhibit distinct regional microrna signatures in mildly dilated ascending aorta, Heart Vessels 32 (6) (2017) 750–767, doi:10.1007/s00380-016-0942-7.
[84] A.D. Corte, L.S. De Santo, S. Montagnani, C. Quarto, G. Romano, C. Amarelli, M. Scardone, M. De Feo, M. Cotrufo, G. Caianiello, Spatial patterns of matrix protein expression in dilated ascending aorta with aortic regurgitation: congenital bicuspid valve versus Marfan's syndrome, J. Heart Valve Disease 15 (1) (2006) 20–27.
[85] N. Choudhury, O. Bouchot, L. Rouleau, D. Tremblay, R. Cartier, J. Butany, R. Mongrain, R.L. Leask, Local mechanical and structural properties of healthy and diseased human ascending aorta tissue, Cardiovasc. Pathol. 18 (2) (2009) 83–91, doi:10.1016/j.carpath.2008.01.001.
[86] T. Pham, C. Martin, J. Elefteriades, W. Sun, Biomechanical characterization of ascending aortic aneurysm with concomitant bicuspid aortic valve and bovine aortic arch, Acta Biomater. 9 (8) (2013) 7927–7936, doi:10.1016/j.actbio.2013.04.021.
[87] Y. Xuan, S.N. D'Souza, Z. Wang, A.S. Pierre, J.S. Lawton, L. Ge, E.E. Tseng, Patient-specific biomechanics in marfan ascending thoracic aortic aneurysms, Ann. Thoracic Surg. (2021), doi:10.1016/j.athoracsur.2021.07.042.